

Solubility behaviour, crystallisation kinetics and pour point: a comparison of linear alkane and triacyl glyceride solute/solvent mixtures

Paul D.I. Fletcher*, Noel A. Roberts and Choephel Urquhart
*Surfactant & Colloid Group, Department of Chemistry,
University of Hull, Hull. HU6 7RX. U.K.*

*Author for correspondence: Prof. P.D.I. Fletcher
E mail: P.D.Fletcher@hull.ac.uk

Abstract

Mixtures of either a hydrocarbon wax in a hydrocarbon solvent or a long chain triacyl glyceride (TAG) in a TAG solvent show complex solubility boundary temperature hysteresis and precipitated crystal network formation leading to gelation. For these industrially-important systems, we show how the equilibrium solubility and its hysteresis, crystallisation kinetics and pour point temperature vary with solute concentration for representative examples of both hydrocarbon (*n*-tetracosane (C₂₄) solute in *n*-heptane (C₇) solvent) and TAG (tristearin (SSS) solute in tricaprylin (CCC) solvent) mixtures. The behaviour is modelled with good accuracy; thereby providing a useful aid to formulation and process optimisation.

Keywords

Alkane, triacyl glyceride, solubility, crystallisation, pour point, crystal network

1. Introduction

When a solution of either a long chain hydrocarbon wax in a short chain hydrocarbon solvent or a solution of a long chain triacyl glyceride (TAG) in a short chain TAG solvent is cooled, solute crystals are formed at temperatures below the solubility boundary temperature of the solution. Upon further cooling, sufficient crystals are produced to form a crystal network throughout the two-phase dispersion of crystals plus saturated solution. The crystal network causes gel formation and the mixture exhibits a finite yield stress and ceases to pour (flow) as a result of gravity [1-3]. The temperature at which this occurs is called the pour point temperature. Improving the understanding of the complex behaviour of these systems is important for many different technological applications. Failure of fuel and crude oils to flow caused by hydrocarbon wax crystallisation is a major problem for pipeline transport of crude oils and the use of hydrocarbon fuels in cold climates. Commercial products such as shoe polish consist of a semi-solid wax crystal network within a matrix of saturated solution. The processing of liquid TAG oil mixtures into semi-solid fat products such as butter and margarine involves the precipitation of the high melting point TAG components, leading to the formation of a gelled fat crystal network which, in turn, determines many key properties of the final semi-solid fat product [4,5].

As a result of their industrial importance, there is extensive background literature on both hydrocarbon and TAG systems. For hydrocarbon systems, studies include measurement and modelling of equilibrium solubilities in alkane mixtures [6-21], alkane crystal nucleation and growth kinetics [22-25] and alkane crystal gel formation [1-3, 26, 27]. Relevant literature on TAG systems includes TAG polymorphism [28-30] and relation to solubility [31], TAG crystallisation (reviews [32-34] and specific TAG systems [35-40]) and fat crystal network and pour point properties [4,5,41]. Most practical applications involve systems containing either mixed hydrocarbon wax solutes in a mixed hydrocarbon solvent or mixed TAG solutes in a mixed TAG solvent. Despite the extensive literature, for both hydrocarbon and TAG systems, there is a lack of systematic investigation of the behaviour of single solute/single solvent mixtures which cover the entire solute concentration range. In particular, the following aspects are currently unclear.

- (i) How does the hysteresis between solubility boundary temperatures measured by heating (T_{heat}) and cooling (T_{cool}) vary with solute concentration and how does this hysteresis relate to the kinetics of crystallisation?
- (ii) How does the pour point temperature (i.e. the temperature at which precipitated crystal network formation causes gelation of the system) vary with solute concentration and how does this relate to the curves of T_{heat} and T_{cool} ?
- (iii) Can we develop a self-consistent model to account for the solute concentration dependences of T_{heat} , T_{cool} and the pour point temperature for both hydrocarbon and TAG systems?

Addressing questions (i) to (iii) for single solute/single solvent systems represents one step towards improving manufacturer's ability to rationally optimise processing conditions for the production of hydrocarbon and TAG systems involving precipitated crystal networks. We note here that extension to complex mixtures would be required for application in many systems of practical interest.

In order to tackle questions (i) to (iii) we have selected two solute/solvent systems which are representative of hydrocarbon and TAG systems of practical interest: *n*-tetracosane (abbreviated to C24) solute in *n*-heptane (abbreviated to C7) solvent and tristearin (abbreviated to SSS) solute in tricaprylin (abbreviated to CCC) as solvent. For each system, we have measured and modelled the inter-linked properties of solubility and its hysteresis, crystallisation kinetics and pour point as functions of solute concentration and discuss the origins of the significant difference in observed behaviour between the hydrocarbon and TAG systems.

2. Experimental

2.1 Materials.

n-tetracosane (abbreviated to C24, Sigma-Aldrich, 99%), *n*-heptane (abbreviated to C7, Fischer Scientific, 99%), tristearin (abbreviated to SSS, Sigma-Aldrich, >99%) and tricaprylin (abbreviated to CCC, Sigma-Aldrich, >99%) were used as received.

2.2 Methods.

Full details of the experimental methods used in the measurement of solubility boundary temperatures (T_{heat} and T_{cool}), pour point temperatures and the extraction and imaging of precipitated crystals are given in ref. [27]. Briefly, solubility boundary temperatures corresponding to the first appearance of crystal precipitates on cooling (T_{cool}) or the maximum temperature at which crystal precipitates were present on heating (T_{heat}) were determined by visual observation of the samples using a 5x magnification hand lens. Pour point temperatures were measured using a slightly modified version of the ASTM D97 procedure [42]. It was taken to be the highest temperature at which no flow of the sample was observed when the vessel was tilted from vertical to horizontal and found to be equal (within the experimental uncertainty of $\pm 0.2^\circ\text{C}$) to the lowest temperature at which movement of the sample was observed on tilting. Solute crystals were extracted by rapid vacuum filtration, dried and sprinkled onto a carbon impregnated 'sticky disc' attached to a 15 mm diameter threaded Hitachi SEM mount. Crystal samples were imaged at various magnifications using an Hitachi TM-1000 SEM operating at 15 kV with a vacuum of 50 Pa.

Powder X-ray diffraction measurements were made using a PANalytical empyrean series 2 powder diffractometer. The X-ray source used is a Cu anode, with radiation wavelengths filtered using a single crystal germanium monochromator, emitting Cu $K\alpha_1$ radiation (wavelength $\lambda = 1.540593 \text{ \AA}$) at the samples. Circular sample holders were used, packed with the powdered material to be analysed. An automatic slit method was used, measuring reflection intensity between angles of 5° and 80° over 15 minutes at controlled room temperature (25°C). Measured intensities were converted to relative intensities by dividing values by the peak diffracted intensity. The diffraction angle θ scale values were converted to a crystal spacing scale according to $\text{spacing} = \lambda / (2\sin(\theta/2))$.

3. Results and Discussion

3.1 Solubility as a function of temperature

Figure 1 shows the variation of solubility boundary temperatures (T_{heat} and T_{cool}) with solute mole fraction for both C24 in C7 and SSS in CCC. It can be seen that the C24/C7 shows a hysteresis in the solubility boundary temperatures (i.e. the difference between T_{heat} and T_{cool}) of only $1\text{-}2^\circ\text{C}$ whereas the SSS/CCC has a much larger hysteresis of approximately 20°C . As discussed in ref. [27], the process of melting of a precipitated crystal (as observed on heating at temperature T_{heat}) is expected to have zero activation energy and so should occur promptly on increasing the temperature. Hence, the measured temperature T_{heat} is expected to correspond to the *equilibrium* solubility boundary temperature. In contrast, the process of crystal precipitation (observed on cooling at temperature T_{cool}) is expected to occur by nucleation and growth and be subject to an activation energy barrier as described below. Hence, crystal precipitation does not occur promptly on cooling below the equilibrium solubility boundary; crystal formation on cooling is fast enough to be observed only when the system is undercooled to a temperature T_{cool} which is significantly below the equilibrium solubility boundary T_{heat} .

The simplest model to quantitatively predict the equilibrium solubility behaviour is based on the assumptions that the solute/solvent mixtures form ideal solutions (i.e. the volume and enthalpy changes of mixing are both zero) and that the wax crystals contain no co-crystallised solvent. In the case of a pure solute which, in the absence of solvent, shows only a single phase transition from crystalline solid to a liquid at a temperature T_{liq} with molar enthalpy change ΔH_{liq} , the variation of solubility with temperature is given by [43-44]:

$$\ln X_{ideal} = \frac{-\Delta H_{liq}}{R} \left(\frac{1}{T} - \frac{1}{T_{liq}} \right) \quad (1)$$

where X_{ideal} is the mole fraction of solute in the ideal saturated solution at absolute temperature T and R is the gas constant. As seen in Table 1, the wax C24 shows more complex phase behaviour [45]. It forms a crystalline solid at temperatures less than T_{rot} at which a rotator phase forms with molar enthalpy change ΔH_{rot} . The rotator phase transforms to the liquid at temperature T_{liq} with molar enthalpy change ΔH_{liq} . To take account of the rotator phase formation, the ideal solution solubility equation must be modified as shown below [9].

$$\ln X_{ideal} = \frac{-\Delta H_{liq}}{R} \left(\frac{1}{T} - \frac{1}{T_{liq}} \right) \quad \text{for } T_{rot} < T < T_{liq} \quad (2)$$

$$\text{and } \ln X_{ideal} - \ln X_{rot} = \frac{-(\Delta H_{liq} + \Delta H_{rot})}{R} \left(\frac{1}{T} - \frac{1}{T_{rot}} \right) \quad \text{for } T < T_{rot} \quad (3)$$

where X_{rot} is the mole fraction of solute in the saturated solution at absolute transition temperature T_{rot} (determined using equation 2).

For the case of solutes having only a single phase transition from solid to liquid but showing slight deviations from ideal behaviour in mixtures with a solvent, equation 1 can be modified to take account of the non-ideality by incorporation of the solute activity coefficient f which is concentration dependent [31]. The coefficient f is defined by $X_{ideal} = fX$ where X_{ideal} is the hypothetical mole fraction of a solute behaving ideally and X is the actual solute mole fraction. For ideal solutions $f = 1$ and $X_{ideal} = X$. For non-ideal solutions according to the regular solution approximation, the activity coefficient f is given by

$$\ln f = \frac{\beta(1-X)^2}{RT} \quad (4)$$

where β is the solute/solvent interaction parameter. Combining equations 2 and 4 followed by some re-arrangement yields equation 5 for the solubility boundary temperature T for a non-ideal solute/solvent system with interaction parameter β .

$$T = \frac{-(\Delta H_{liq} + \beta(1-X)^2)}{R \left(\ln X - \frac{\Delta H_{liq}}{RT_{liq}} \right)} \quad (5)$$

Using literature values of the transition temperatures and enthalpies [45,46] given in Table 1, equations 2, 3 and 5 were used to model the equilibrium solubility boundaries measured for the two solute /solvent systems. From the calculated curves in Figure 1, it can be seen that the C24/C7 system shows ideal behaviour; using no adjustable parameters, the agreement between measured and calculated solubility temperatures is within the estimated uncertainties of ± 0.5 °C. For TAG systems, the situation is complicated by the fact that, in general, TAG crystals can form in either the

α , β or β' polymorphs. Using literature values of the transition temperatures and enthalpies for all three polymorphs [46] given in Table 1, the experimental equilibrium solubility boundary for the SSS/CCC system is compared with ideal and regular solution predicted curves for the three polymorphs in Figure 1. It can be seen that the measured equilibrium solubility boundary (i.e. T_{heat}) shows good agreement with the regular solution model calculations based on the β polymorph being formed and a fitted interaction parameter of +1910 J mol⁻¹. As seen in Figure 1, this best-fit value of β corresponds to a rather small deviation from ideal behaviour.

As shown in Figure 2, XRD measurements confirm that the SSS crystals produced under the various crystal precipitation conditions used were all exclusively the β polymorph. The β polymorph is produced exclusively despite the fact that the T_{cool} curve lies below the estimated equilibrium solubility boundary of the β' polymorph.

3.2 Crystallisation kinetics

As discussed above, the true equilibrium solubility boundary temperature corresponds to T_{heat} . When a solution is cooled from a temperature above T_{heat} to a temperature between T_{heat} and T_{cool} , the equilibrium state corresponds to precipitated crystals plus saturated solution but the systems remains as a metastable, single-phase solution as the kinetics of the crystal formation are slow due to the activation energy required for crystal nucleation and growth. Figure 3 shows an example of experimental measurements of the times required for the first crystals to be observed following cooling of a solution to a temperature T within the metastable range between T_{heat} and T_{cool} . It can be seen that the induction time τ required to first form visible crystals at an incubation temperature T depends very strongly on the extent of undercooling, i.e. $(T_{\text{heat}} - T)$.

According to homogeneous nucleation theory [32-34,47,48], the Gibbs free energy of formation of a solute cluster (assumed spherical) from dissolved solute monomers shows a maximum at a critical nucleus radius r^* , which is given by

$$r^* = \frac{2\gamma v T_{\text{heat}}}{\Delta H_{\text{liq}} \Delta T} \quad (6)$$

where γ is the crystal nucleus-saturated solution interfacial tension, v is the molar volume of the crystal and ΔT is the extent of undercooling, i.e. $(T_{\text{heat}} - T)$. The Gibbs free energy of formation of critical nucleus of radius r^* is given by

$$\Delta G^* = \frac{16\pi\gamma^3 v^2 T_{\text{heat}}^2}{3\Delta H_{\text{liq}}^2 \Delta T^2} \quad (7)$$

It is assumed here that the induction time τ is given by an equation of the form

$$\tau \approx a \exp\left(\frac{\Delta G^*}{kT}\right) \quad (8)$$

where a is pre-exponential factor assumed to be approximately constant for all ΔT and k is Boltzmann's constant. Combining equations 7 and 8 and taking logarithms gives

$$\ln\tau = \ln a + \left(\frac{16\pi\gamma^3 v^2}{3\Delta H_{\text{liq}}^2 kT}\right) \frac{T_{\text{heat}}^2}{\Delta T^2} \quad (9)$$

The variation of T (a few °C for the range of ΔT measured for each system) causes negligible change in the bracketed term relative to the variation of $\frac{T_{\text{heat}}^2}{\Delta T^2}$. Hence, a graph of $\ln\tau$ versus $\frac{T_{\text{heat}}^2}{\Delta T^2}$ should give a straight line plot from which the gradient yields an estimate of the crystal nucleus-saturated solution interfacial tension γ . This type of plot is an alternative to the Fisher-Turnbull [47] plot of $\ln(\tau T)$ versus $1/[T(\Delta T)^2]$ which is applicable to single component systems rather than solute/solvent mixtures.

Plots according to equation 9 are shown in Figure 4 for different concentrations of C24 in C7 and SSS in CCC. It can be seen that the experimental data is reasonably well described by the form of equation 9, i.e. $\ln\tau$ is proportional to $\frac{T_{\text{heat}}^2}{\Delta T^2}$. However, it is important to note that classical nucleation theory has several shortcomings and unresolved issues when attempting to ascribe physical meaning to the best-fit intercepts and gradients for the systems investigated here. Firstly, it is uncertain whether nucleation occurs homogeneously or heterogeneously. If heterogeneous nucleation is occurring, $\ln\tau$ is still predicted to be proportional to $\frac{T_{\text{heat}}^2}{\Delta T^2}$ but the physical meaning of the gradient of the plot is different. Secondly, the physical meaning of the crystal-saturated solution tension γ is unclear since the nuclei are not expected to be spherical and the tensions of the different crystal faces of the critical nucleus will, in general, be different. Thirdly, the measured values of τ correspond to the times at which crystals are first observed to appear using hand lens magnification. Thus, the values might be expected to include contributions from both nucleation and growth of the crystals. Noting these significant caveats, equation 9 is best regarded as a semi-empirical fitting function which enables a parameterisation of this type of crystallisation kinetic data. Despite these shortcomings, analysis of the concentration-averaged gradients of Figure 4 yields estimates of the *apparent* or *effective* values of γ which are 4 and 0.9 mJ m⁻² for the SSS/CCC and C24/C7 systems respectively. This suggests that the larger solubility temperature hysteresis (i.e. $T_{\text{heat}} - T_{\text{cool}}$) for the TAG systems mainly results from its higher value of the effective crystal nucleus-solution tension. However, using equation 6 with the values of γ estimated in this way, yields critical nucleus radius r^* values of 0.7-0.8 (corresponding to approximately 1 SSS molecule) and 0.9-1.9 nm (corresponding to 4-39 C24 molecules) for the SSS/CCC and C24/C7 systems respectively. The apparent critical nucleus size estimated in this way for the TAG system is clearly physically unrealistic and highlights that equation 9 is best regarded as a semi-empirical fitting function.

Despite the semi-empirical nature of the kinetic analysis, it is almost certainly true that the major factor determining the crystallisation kinetics is the effective γ since the free energy barrier to nucleation is proportional to γ^3 . The values estimated here (4 and 0.9 mJ m⁻² for the SSS/CCC and C24/C7 systems respectively) can be compared with literature values estimated from crystallisation kinetics for related alkane and TAG systems. Turnbull and Cormia [22] and Kraack et al. [24] report tension values of approximately 8 mJ m⁻² for pure C24 whereas Mota et al. [25] estimate values of approximately 0.4 to 1.3 mJ m⁻² for a range of middle distillate fuel oils containing approximately 20 wt% n-paraffins. The value we report here for C24/C7 mixtures of 0.9 mJ m⁻² is approximately 10-fold lower than for pure C24 in a melt but similar to values relevant to paraffin wax precipitation from a solvent. For TAG systems, Campos et al. [38] estimate tensions in the range 1.3 to 1.9 mJ m⁻² for cocoa butter blended with either trilaurin or tristearin. Ahmadi et al. [39] report values in the range 0 to 5 mJ m⁻² (dependent on solid fat content) for mixtures of fully hydrogenated canola oil (which has a high SSS content) and high oleic sunflower oil (which has a high triolein content).

Because of the unresolved issues relating to the kinetic analysis and the lack of systematic literature data for systems directly comparable with those used here, it is of interest to investigate alternative

methods to estimate the relative magnitudes of the crystal-solution tensions for alkane and TAGs. Although it is not possible to measure solid-liquid surface tensions directly, one can use a theoretical approach based on estimation of the dispersive and polar components of the excess surface energies. According to Fowkes [49] and Owens and Wendt [50], the surface tension of a condensed phase against air γ can be expressed as the sum of components due to dispersion forces γ^d and polar forces γ^p according to:

$$\gamma = \gamma^d + \gamma^p \quad (10)$$

The interfacial tension between two condensed phases a and b is then expressed in terms of these two components for each phase.

$$\gamma_{ab} = \gamma_a + \gamma_b - 2\sqrt{\gamma_a^d \gamma_b^d} - 2\sqrt{\gamma_a^p \gamma_b^p} \quad (11)$$

Using equations 10 and 11 and Young's equation, values of γ^d and γ^p for solid-air surfaces can be derived from measurements of contact angles formed by drops of a range of liquids with known surface tensions placed on the solid surface [51]. To estimate the crystal nuclei-solution tensions, we use literature values of the solvent-air and solvent-water tensions [52-55] as shown in Table 2.

Using literature values of γ^d and γ^p for the water-air surface [56] (Table 2), γ^d and γ^p values for the liquid-air surfaces of both CCC and C7 were derived using equations 10 and 11. These values were then combined with literature values of γ^d and γ^p for the SSS-air⁵⁷ and C24-air [54] surfaces to obtain the values of the solid SSS-CCC and solid C24-C7 interfacial tensions which were found to be 1.9 and 0.8 mJ m⁻² respectively. Hence, the results of this approach offer some support to the conclusion that the TAG system tension (and hence the nucleation energy barrier) is higher than for the alkane system. However, it should be noted that ref. [57], from which the surface energy component data for the SSS-air surface was taken, does not specify the SSS polymorph used. This factor may contribute to the observed discrepancy between the TAG system tensions estimated by the two methods. For a fuller discussion of the relative merits of different methods for the determination of solid-liquid tensions and a comparison of values obtained for a wide range of solid/liquid systems, the reader is directed to the review by Wu and Nancollas [58].

The fitting of equation 9 to the kinetic data provides a basis for estimating the variation of T_{cool} with solute concentration as follows. Equation 9 has the form

$$\ln \tau = \ln a + b \left(\frac{T_{heat}^2}{\Delta T^2} \right) \quad (12)$$

where $\ln a$ is the intercept and b is the gradient of the plots shown in Figure 4. The measured values of T_{cool} are the temperatures at which crystals appear within an observation time τ_{cool} and hence we set τ to be τ_{cool} when $T = T_{cool}$. The constant a corresponds to the value of τ when the undercooling ΔT is infinite and there is zero energy barrier to nucleation. Under these conditions, the time for visible crystal formation is likely to depend on solute concentration and may be controlled either by solute diffusion or by slow molecular re-arrangement during attachment to the growing crystal. From the best fit values of $\ln a$ shown in Figure 4, it can be seen (i) a is smaller for SSS in CCC as compared with C24 in C7 and (ii) a decreases with increasing solute concentration. If the nucleation with zero energy barrier was diffusion controlled, then the constant a should be larger for the SSS/CCC system since the viscosity of CCC [52,59] is approximately 28-fold larger than for C7 [54]. In fact, the constant a is smaller for the SSS/CCC system which suggests that nucleation in these systems is not diffusion controlled. Secondly, since it appears that the value of a varies with

solute concentration, we can recast equation 12 to include a solute concentration dependence (by analogy with chemical reaction kinetic rate laws) by substituting $a = A[\text{solute}]^{-n}$ where A is a constant and n corresponds to nucleation rate order with respect to the solute. Substituting $\tau = \tau_{\text{cool}}$ when $T = T_{\text{cool}}$ gives:

$$\ln(\tau_{\text{cool}}) = \ln\{A[\text{solute}]^{-n}\} + b \left(\frac{T_{\text{heat}}^2}{(T_{\text{heat}} - T_{\text{cool}})^2} \right) \quad (13)$$

which, on re-arrangement, gives

$$T_{\text{cool}} = T_{\text{heat}} - \sqrt{\frac{bT_{\text{heat}}^2}{\ln\tau_{\text{cool}} - \ln(A[\text{solute}]^{-n})}} \quad (14)$$

Figure 5 shows a comparison of measured values of T_{cool} with those fitted using equation 14. For the fitting, the values of τ_{cool} were set at 3 minutes for the SSS/CCC system and 9 minutes for the C24/C7 system, reflecting the times used in the measurements of T_{cool} . The values of b were set as the concentration averaged values and the values of A were taken as the concentration averaged values of $a/[\text{solute}]^{-n}$ for each system from Figure 4. Only the value of n was floated. Reasonable agreement between the experimental and calculated curves is observed with values of n equal to approximately 0.8 for the SSS/CCC and 0.7 for the C24/C7 systems respectively. Overall, the variation of T_{cool} with solute concentration is well described using the crystallisation kinetic fitting parameters with the incorporation of a solute concentration dependence of a .

3.3 Pour point temperatures

On cooling, precipitation of either alkane or TAG solutes leads to the formation of a crystal network which causes cessation of flow at the pour point temperature T_{pp} . In a previous study [27] of alkane wax solutes in an alkane solvent, we have shown the variation of T_{pp} with solute concentration corresponds to the temperature at which a critical solute mole fraction X^* has precipitated. Thus, for a solute behaving ideally, T_{pp} varies with overall solute mole fraction X according to

$$T_{\text{pp}} = \frac{-\Delta H_{\text{liq}}}{R \left(\ln(X - X^*) - \left(\frac{\Delta H_{\text{liq}}}{RT_{\text{liq}}} \right) \right)} \quad (15)$$

Similar replacement of X by $(X - X^*)$ in equations 3 or 5 leads to related expressions for T_{pp} for either systems with additional phase transitions or regular solutions. For a particular solute/solvent system, the value of X^* is independent of overall solute concentration but is specific to that system. It is important to note that equation 15 is only valid when $T_{\text{pp}} < T_{\text{cool}}$, i.e. when the amount of crystals formed is controlled only by *equilibrium* considerations and is not limited by the *kinetics* of crystal formation.

Figure 6 shows the variation of T_{pp} with solute concentration in relation to the equilibrium solubility boundary (T_{heat}) and the lower limit of the metastable region (T_{cool}) for both the SSS/CCC and C24/C7 systems. For the C24/C7 system (lower plot), it can be seen that T_{pp} lies below T_{cool} for C24 concentrations less than approximately 30 wt%. In this *equilibrium* regime, the measured values of T_{pp} show good agreement with the appropriate form of equation 15 with X^* corresponding to 8.5 wt%. For C24 concentrations greater than 30 wt%, the fitted pour point transition temperature lies above T_{cool} . In this *metastable* or *kinetic* regime, the pour point transition is limited by the crystallisation kinetics and occurs promptly when the solution is cooled to T_{cool} . For the SSS/CCC

system (upper plot), the equilibrium regime in which $T_{pp} < T_{cool}$ only extends to approximately 12 wt% and is additionally complicated by freezing of the CCC solvent at 5 °C. The solid curve shows the variation of T_{pp} predicted to occur if $X^* = 12$ wt% and if the system equilibrium regime extended over the whole concentration range. In reality, the system is within the equilibrium regime only in a very narrow concentration range around 12 wt%. At lower concentrations, the measured T_{pp} corresponds to the freezing point of the solvent; at higher concentrations in the metastable regime, the measured T_{pp} is equal to T_{cool} . The comparison of the two systems shows how the slower crystallisation kinetics of the TAG system greatly extends the metastable regime and thereby obscures the equilibrium regime behaviour of T_{pp} seen for the alkane system. Within the equilibrium regime, the measured pour point corresponds to the point at which the *minimum* amount of crystals required to prevent flow have formed. In the metastable or kinetic regime, the amount of crystals formed at the observed pour point will exceed this minimum amount.

From Figure 6, the minimum amounts of crystals required to prevent flow and cause the pour point transition $X^* = 8.5$ and $X^* = 12$ wt% for C24 and SSS respectively. These values correspond to critical crystal volume fractions ϕ^* of 0.074 and 0.11. The factors determining ϕ^* for gel formation by crystal networks are currently not fully resolved but are likely to include the crystal size, shape and strength of mutual adhesion. In a previous study [27], it was shown that ϕ^* values for different alkane wax/alkane solvent systems correlate weakly with the volume fraction at which the volumes of revolution of the crystal overlap $\phi_{overlap}$ where $\phi_{overlap} \approx 1.1(h/d)$ for plate-like crystals of thickness h and diameter d . Using dimensions estimated from SEM images of crystals extracted from alkane wax/solvent mixtures, it was found that $2.5(h/d) < \phi^* < 11(h/d)$ for a range of systems with and without pour point depressant polymer additives.

With this background in mind, we show SEM images of C24 and SSS crystals extracted from mixtures with solvent at temperatures between T_{cool} and T_{pp} . The C24 crystals are isolated, thin, irregularly shaped plates with average thickness h 0.8 μm and average longest dimension d of 120 μm . The average value of (h/d) is approximately 0.007 and so ϕ^* of 0.074 equates to approximately $11(h/d)$ in this case. The SSS (β form) crystals have a plank-like shape with an approximate average thickness of 1.5 μm . They are not isolated, individual crystals but appear to grow from a common base which makes it impossible to estimate the longest dimension of a single crystal. This different growth habit suggests that the mechanism of the gel formation and pour point transition does not occur by overlap and adhesion between separate SSS crystals; rather the fat crystal network is formed by connected crystals. Detailed experimental and simulation studies [61,62] of crystal network formation in TAG solute/solvent systems indicate initial formation of TAG crystal nanoplatelets with dimensions in the range 30-370 nm followed by their self-assembly to produce a crystal network of complex 3D structure. As described ref. [61], TAG nanoplatelet crystals were observed following an extraction procedure involving suspension in cold isobutanol and high shear homogenisation. The SSS crystals shown in Fig. 7 were extracted by rapid vacuum filtration and so were not subject to the high shear required to observe nanoplatelet crystals. Although the precise mechanistic sequence of precipitation, crystal “jamming” and/or self assembly to form the final, gelled, crystal network state remains elusive, it seems plausible to suggest that the different appearances of the alkane and TAG crystals (isolated versus connected) seen in Figure 7 may be related to the different regimes in which the pour point transition occurs, i.e. fast crystallisation with the amount of crystals limited by equilibrium considerations for the alkane and slow crystal formation limited by kinetics for the TAG.

Conclusions

For examples of both hydrocarbon and TAG solute/solvent systems, we have shown:

1. The equilibrium solubility boundary corresponds to the temperature at which the last crystals melting on heating the mixtures (T_{heat}). The variation of T_{heat} with solute concentration is accurately modelled on the basis that C24 forms ideal solutions in C7 whereas SSS solutions in CCC are slightly non-ideal.
2. When solutions of either system are cooled from above to below T_{heat} , the logarithm of the time for crystal formation $\ln\tau$ is proportional to $(T_{\text{heat}} - T)^{-2}$. Crystal formation kinetics are much slower for SSS compared with C24 and correspond to effective values of the crystal nucleus-solution tension of 4 and 0.9 mJ m⁻² for the SSS/CCC and C24/C7 systems respectively.
3. As a result of the crystallisation kinetics, the hysteresis in solubility boundary temperatures between heating (T_{heat}) and cooling (T_{cool}) is small for the alkane system but large for the TAG system. We have shown how the variation of T_{cool} with solute concentration can be accurately modelled using parameters from crystallisation kinetic measurements with the incorporation of a concentration dependence term in the pre-exponential factor.
4. In both systems, there are two regimes of pour point behaviour. In the equilibrium regime, the pour point temperature $T_{\text{pp}} < T_{\text{cool}}$ and corresponds to the temperature at which the minimum concentration of solute crystals required to cause the pour point transition X^* has precipitated. In the metastable or kinetic regime, the pour point transition is controlled by the crystallisation kinetics and occurs promptly at T_{cool} . The value of X^* is 8.5 wt% for the C24/C7 system for which the equilibrium regime is relatively large and 12 wt% for the SSS/CCC system in which the equilibrium regime is very narrow.

The ability to accurately model the key system temperatures (T_{heat} , T_{cool} and T_{pp}) all as a function of solute concentration is important in the formulation and process optimisation of a wide range of hydrocarbon and TAG systems. The approaches demonstrated and validated here for examples of both hydrocarbon and TAG single solute/single solvent systems is capable of extension to more complex multicomponent mixtures of practical interest.

Acknowledgements

We thank Lubrizol, Hazelwood, UK for provision of a PhD studentship for Noel A. Roberts. We also wish to acknowledge the use of the EPSRC funded National Chemical Database Service hosted by the Royal Society of Chemistry.

References

- [1] D.J. Abdallah and R.G. Weiss, *Langmuir*, 2000, **16**, 352-355.
- [2] R.F.G. Visintin, R. Lapasin, E. Vignati, P. D'Antona and T.P. Lockhart, *Langmuir*, 2005, **21**, 6240-6249.
- [3] E. Vignati, R. Piazza, R.F.G. Visintin, R. Lapasin, P. D'Antona and T.P. Lockhart, *J. Phys. Condens. Matter*, 2005, **17**, S3651-S3660.
- [4] Structure and Properties of Fat Crystal Networks, Second Ed., A.G. Marangoni and L.H. Weddorp, CRC Press, Boca Raton, 2012.
- [5] A.G. Marangoni, N. Acevedo, F. Maleky, E. Co, F. Peyronel, G. Mazzanti, B. Quinn and D. Pink, *Soft Matter*, 2012, **8**, 1275-1300.
- [6] H.E.L. Madsen and R. Boistelle, *J. Chem. Soc. Faraday Trans. 1*, 1976, **72**, 1078-1081.
- [7] S-S. Chang, J.R. Maurey and W.J. Pummey, *J. Chem. Eng. Data*, 1983, **28**, 187-189.
- [8] M-C. Haulait-Pirson, G. Huys and E. Vanstraelen, *Ind. Eng. Chem. Res.*, 1987, **26**, 447-452.
- [9] U. Domanska and J. Rolinska, *Fluid Phase Equilibria*, 1989, **45**, 25-38.
- [10] J.A.P. Coutinho, S.I. Andersen, E. H. Stenby, *Fluid Phase Equilib.*, 1995, **103**, 23-39.
- [11] C. Lira-Galeana, A. Firoozabadi and J.M. Prausnitz, *AIChE J.*, 1996, **42**, 239-248.
- [12] J. Pauly, C. Daupohin and J.L. Daridon, *Fluid Phase Equilib.*, 1998, **149**, 191-207.
- [13] E. Provost, V. Chevallier, M. Bouroukba, D. Petitjean and M. Dirand, *J. Chem. Eng Data*, 1998, **43**, 745-749.
- [14] P.M. Ghogomu, E. Provost, M. Bouroukba, M. Dirand and M. Hoch, *J. Thermal Anal.*, 1998, **53**, 49-56.
- [15] S. Kato, D. Hoshino, H. Noritomi and K. Nagahama, *Fluid Phase Equilib.*, 2004, **219**, 41-47.
- [16] J.A.P. Coutinho, C. Goncalves, I.M. Marrucho, J. Pauly and J-L. Daridon, *Fluid Phase Equilib.*, 2005, **233**, 28-33.
- [17] J.A.P. Coutinho, F. Mirante and J. Pauly, *Fluid Phase Equilib.*, 2006, **247**, 8-17.
- [18] J.A.P. Coutinho, B. Edmonds, T. Morwood, R. Szczepanski and X. Zhang, *Energy & Fuels*, 2006, **20**, 1081-1088.
- [19] B. Coto, C. Martos, J.J. Espada, M.D. Robustillo and J.L. Pena, *Fuel*, 2010, **89**, 1087-1094.
- [20] E. Ghanaei, F. Esmaeilzadeh and J. Fathikalajahi, *Fuel*, 2012, **99**, 235-244.
- [21] W. Wang, K. Wu, J. Duan, P. Wang and J. Gong, *Adv. Mech. Eng.*, 2013, article ID:829591, 1-8.
- [22] D. Turnbull and R.L. Cormia, *J. Chem. Phys.*, 1961, **34**, 820-831.
- [23] E.B. Sirota, *J. Chem. Phys.*, 2000, **112**, 492-500.
- [24] H. Kraack, E.B. Sirota and M. Deutsch, *J. Chem. Phys.*, 2000, **112**, 6873-6885.
- [25] F.L. Mota, S. Teychene and B. Biscans, *Ind. Eng. Chem. Res.*, 2014, **53**, 2811-2819.
- [26] M. Senra, T. Scholand, C. Maxey and H.S. Fogler, *Energy & Fuels*, 2009, **23**, 5947-5957.
- [27] B.P. Binks, P.D.I. Fletcher, N.A. Roberts, J. Dunkerley, H. Greenfield, A. Mastrangelo and K. Trickett, *Phys. Chem. Chem. Phys.*, 2015, **17**, 4107-4117.
- [28] D. Chapman, *Chem. Rev.*, 1962, **62**, 433-456.
- [29] J.R. Dafler, *J. Amer. Oil Chem. Soc.*, 1977, **54**, 249-254.
- [30] E. M. Barrall and J.C. Guffy, Chap. 1, pp 1-12 in *Ordered Fluids and Liquid Crystals*, Eds. R.S. Porter and J.F. Johnson, Adv. Chem. Series, Vol. **63**, 1967, Amer. Chem. Soc.
- [31] P. Bennema, J. van Eupen, B.M.A. van der Wolf, J.H. Los and H. Meekes, *Int. J. Pharm.*, 2008, **351**, 74-91.
- [32] K. Sato, *Chem. Eng. Sci.*, 2001, **56**, 2255-2265.
- [33] C. Himawan, V.M. Starov and A.G.F. Stapley, *Adv. Colloid Interface Sci.*, 2006, **122**, 3-33.
- [34] M.J.W. Povey, *Food Hydrocolloids*, 2014, **42**, 118-129.
- [35] N. Gartti, E. Wellner and S. Sarig, *J. Amer. Oil Chem. Soc.*, 1982, **59**, 181-185.
- [36] S.K. Singh, A.F. Jalali and M. Alden, *J. Amer. Oil Chem. Soc.*, 1999, **76**, 507-510.

- [37] W. Kloek, P. Walstra and T. van Vliet, *J. Amer. Oil Chem. Soc.*, 2000, **77**, 389-398.
- [38] R. Campos, M. Ollivon and A.G. Marangoni, *Crystal Growth & Design*, 2010, **10**, 205-217.
- [39] L. Ahmadi, A.J. Wright and A.G. Marangoni, *Food Biophysics*, 2009, **4**, 64-76.
- [40] F. Pattarino, R. Bettini, S.F. Bonda, A.D. Bella and L. Giovannelli, *Int. J. Pharm.*, 2014, **473**, 87-94.
- [41] K. Higaki, Y. Sasakura, T. Koyano, I. Hachiya and K. Sato, *J. Amer. Oil Chem. Soc.*, 2003, **80**, 263-270.
- [42] ASTM. Designation: D97-09 Standard test method for pour point of petroleum products. 2009.
- [43] I.Z. Schroder, *Z. Physik. Chem.*, 1893, **11**, 449-465.
- [44] H. Le Chatelier, *Compte. Rend.*, 1894, **118**, 638-641.
- [45] M. Dirand, M. Bouroukba, V. Chevallier, D. Petitjean, E. Behar and V. Ruffier-Meray, *J. Chem. Eng. Data*, 2002, **47**, 115-143.
- [46] E. Da Silva, S. Bresson and D. Rousseau, *Chem. Phys. Lipids*, 2009, **157**, 113-119.
- [47] D. Turnbull and J.C. Fisher, *J. Chem. Phys.*, 1949, **17**, 71-73.
- [48] I. Foubert, K. Dewettinck and P.A. Vanrolleghem, *Trends Food Sci. & Technol.*, 2003, **14**, 79-92.
- [49] Fowkes, F.M. *J. Phys. Chem.*, **1963**, **67**, 2538.
- [50] Owens, D.K.; Wendt, R.C. *J. Appl. Polym. Sci.*, **1969**, **13**, 1741.
- [51] van Oss, C.J. *Interfacial forces in aqueous media*, New York: Marcel Dekker, **1994**
- [52] J.W. Goodrum and M.A. Eitcman, *Bioresource Technol*, 1996, **56**, 55-60
- [53] B.P. Binks and A. Desforges, *Langmuir*, 2007, **23**, 1098-1106.
- [54] Selected values of properties of hydrocarbons and related compounds, Thermodynamics Research Center AP144 Hydrocarbon Project, C.W. Haas (Ed.), Thermodynamic Research Center, Texas A&M University College Station, Texas, 1978.
- [55] S. Zeppieri, J Rodriguez, AL Lopez de Ramos, *J. Chem. Eng. Data*, 2001, **46**, 1086-1088
- [56] Jasper, J.J. *J. Phys. Chem. Ref. Data*, **1972**, **1**, 841.
- [57] M. Saito and A. Yabe, *Textile Res. J.*, 1984, **54**, 18-22.
- [58] W. Wu and G.H. Nancollas, *Adv. Colloid Interface Sci.*, 1999, **79**, 229-279.
- [59] S.M. Ghazani, D.A. Pink, M. Koutchekinia, J.R. Carney, R. Bond, W. Rakitsky and A.G. Marangoni, *RSC Adv.*, 2015, **5**, 37180-37187.
- [60] N.C. Acevedo and A.G. Marangoni, *Crystal Growth & Des.*, 2010, **10**, 3327-3333.
- [61] F. Peyronel, D.A. Pink and A.G. Marangoni, *Curr. Opinion Colloid Interface Sci.*, 2014, **19**, 459-470.

Table 1. Phase transition temperatures and enthalpy changes for the three pure waxes used here. The data for C24 is taken from ref. [45]; data for SSS is from ref. [46].

Wax	T _{rot} / °C	T _{liq} / °C	ΔH _{rot} / J mol ⁻¹	ΔH _{liq} / J mol ⁻¹
Tetracosane C24	47.6	50.5	31701	54396
Tristearin SSS (α form)	-	54.9	-	115357
Tristearin SSS (β' form)	-	65.3	-	144776
Tristearin SSS (β form)	-	72.4	-	193451

Table 2. Measured surface tensions and derived dispersion and polar surface energy components (at 20 °C) used to estimate crystal nucleus-solution tensions.

interface	γ _{measured} /mJ m ⁻²	γ ^d /mJ m ⁻²	γ ^p /mJ m ⁻²
CCC-air	29.9	27.45	2.45
CCC-water	31.0	-	-
C7-air	20.14	20.14	0
C7-water	51.20	-	-
Water-air	71.9	21.5	50.4
SSS-air (polymorph not stated)	21.8	21.7	0.1
C24-air (actually C20 as undercooled liquid)	28.9	28.9	0

Figure 1. Variation of solubility with temperature for SSS in CCC (upper plot) and C24 in C7 (lower plot). Solid curves are calculated according to ideal solution theory and the dashed curve correspond to regular solution theory. For the SSS/CCC systems, calculated curves are shown for the α , β' and β polymorphs. For each plot, unfilled circles correspond to measured values of T_{heat} and filled circles show T_{cool} values.

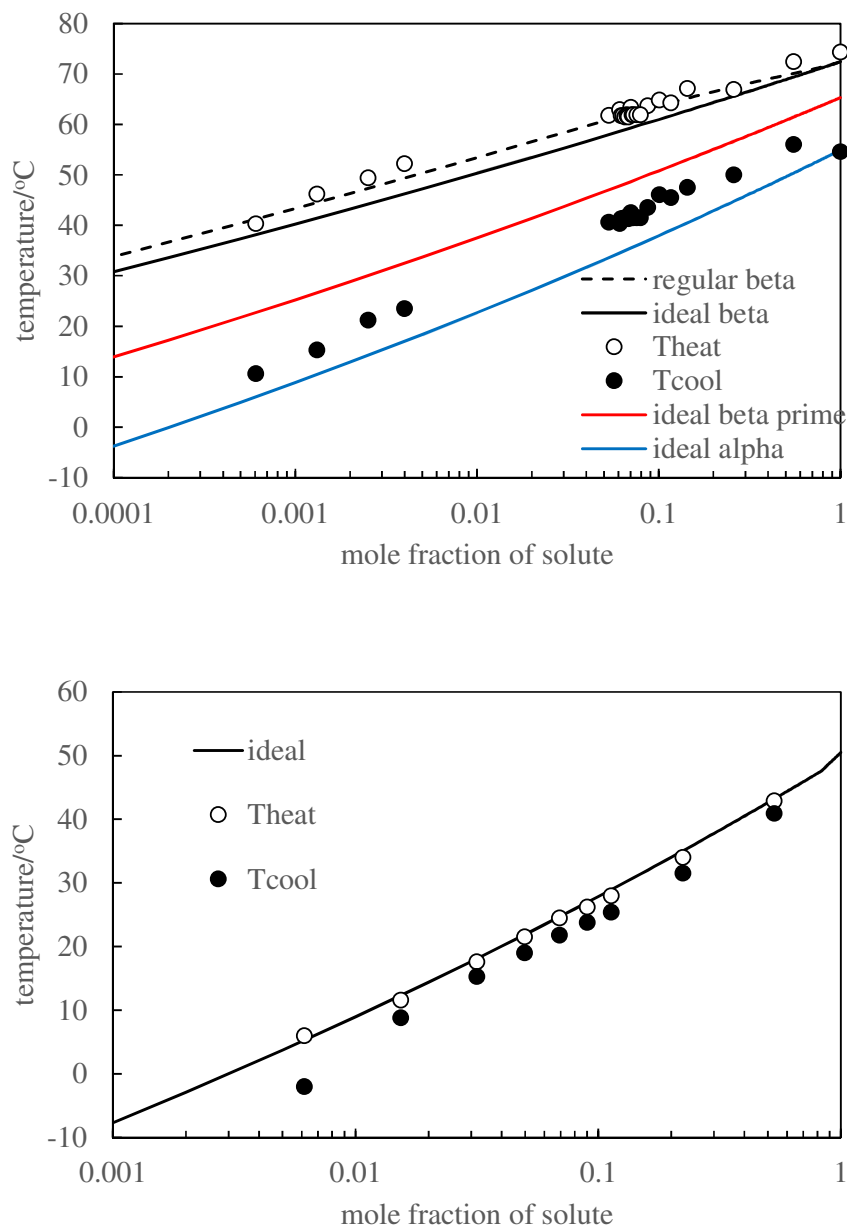


Figure 2. XRD plots for SSS crystals measured for three samples (“as received”, as extracted from a 10 wt% solution upon cooling just below T_{cool} at 0.5 °C/min (denoted “0.5 °C/min”) and as extracted from a 10 wt% solution cooled at 2.0 °C/min to 1.0 °C above T_{cool} and held for three hours prior to extraction (denoted “Held above T_{cool} ”)) and compared to literature data [40,46]. The vertical solid lines indicate the major peak positions for the β polymorph; the vertical dotted line corresponds to the major peak for the α polymorph (absent) and the vertical dashed lines correspond to the β' polymorph (absent).

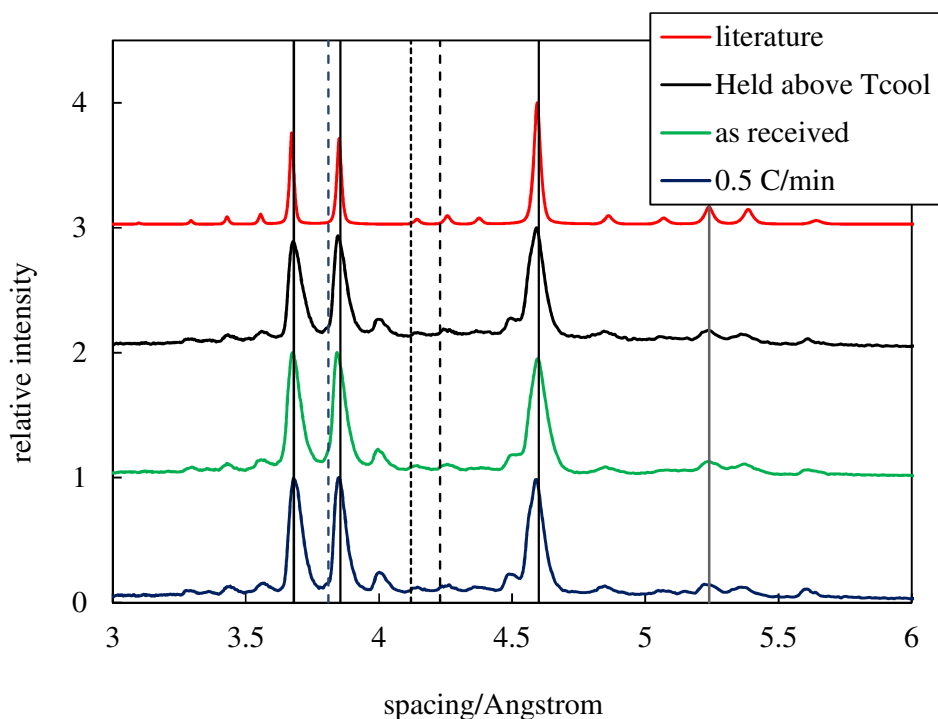


Figure 3. Variation of crystal appearance time for 10 wt% SSS in CCC for samples cooled to different temperatures between T_{heat} and T_{cool} , shown as the vertical dashed lines. Unfilled circles shows observations for which no crystals were present; filled circles indicate crystals were present. The solid curve is calculated according to the linear fits shown in Figure 4.

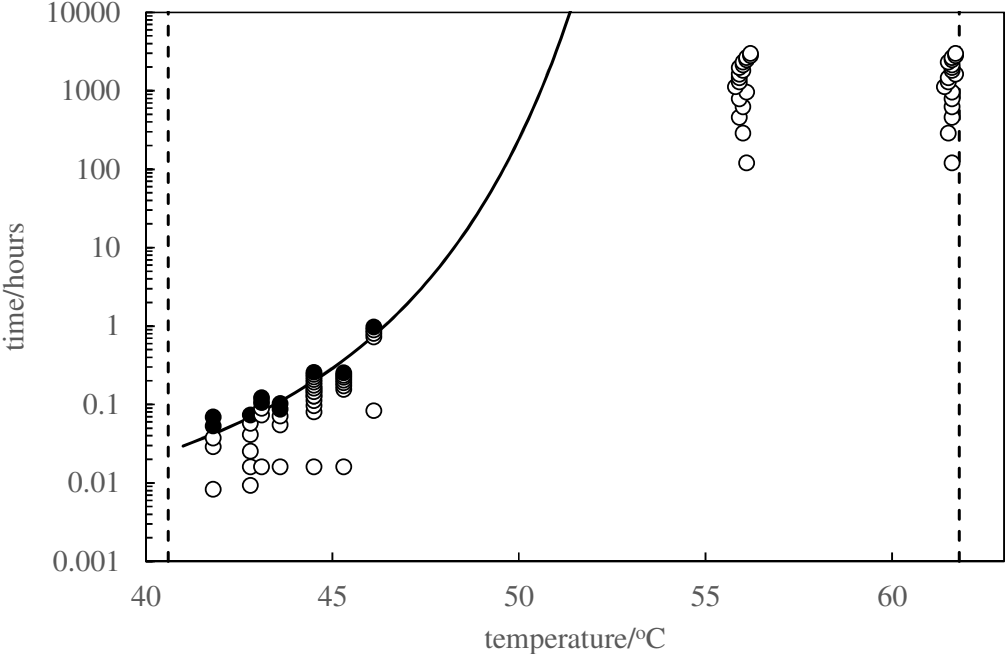


Figure 4. Fits of the crystallisation kinetic data according to equation 9. Best-fit values of intercept ($\ln a$) and gradient (b) and the correlation coefficients are: 10 wt% C24: -3.27, 1.44×10^{-4} , 0.993; 15 wt% C24: -3.23, 1.09×10^{-4} , 0.986; 20 wt% C24: -6.08, 5.09×10^{-4} , 0.983; 10 wt% SSS: -7.80, 1.65×10^{-2} , 0.937, 15 wt% SSS: -9.24, 2.21×10^{-2} , 0.999 and 20 wt% SSS: -9.39, 2.19×10^{-2} , 0.973.

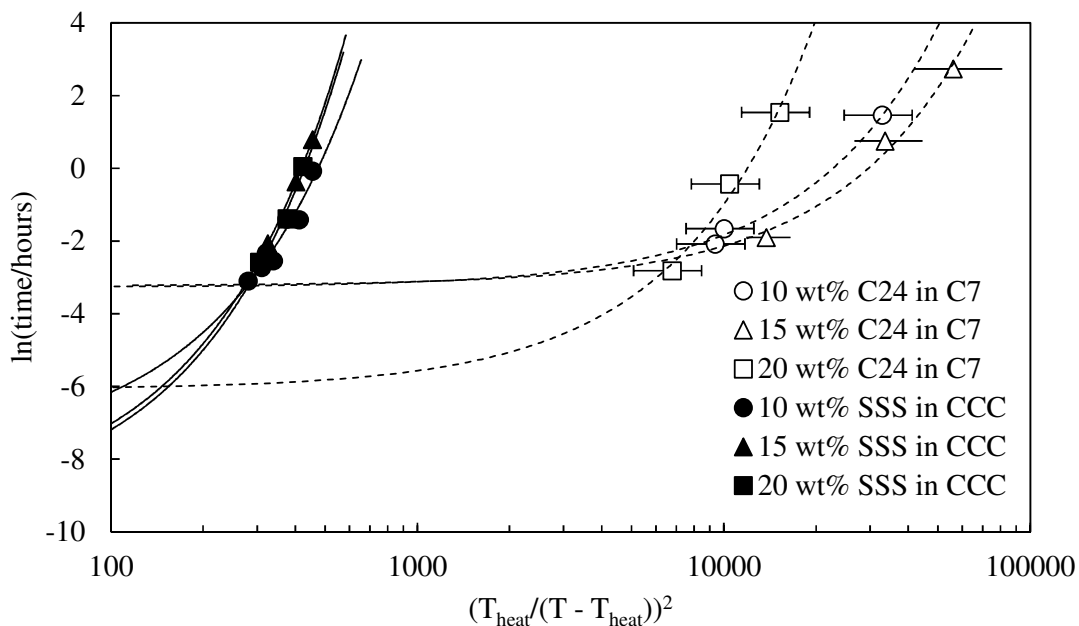


Figure 5. T_{cool} versus solute concentration fitted according to the crystallisation kinetic data fitting parameters for SSS in CCC (upper plot) and C24 in C7 (lower plot).

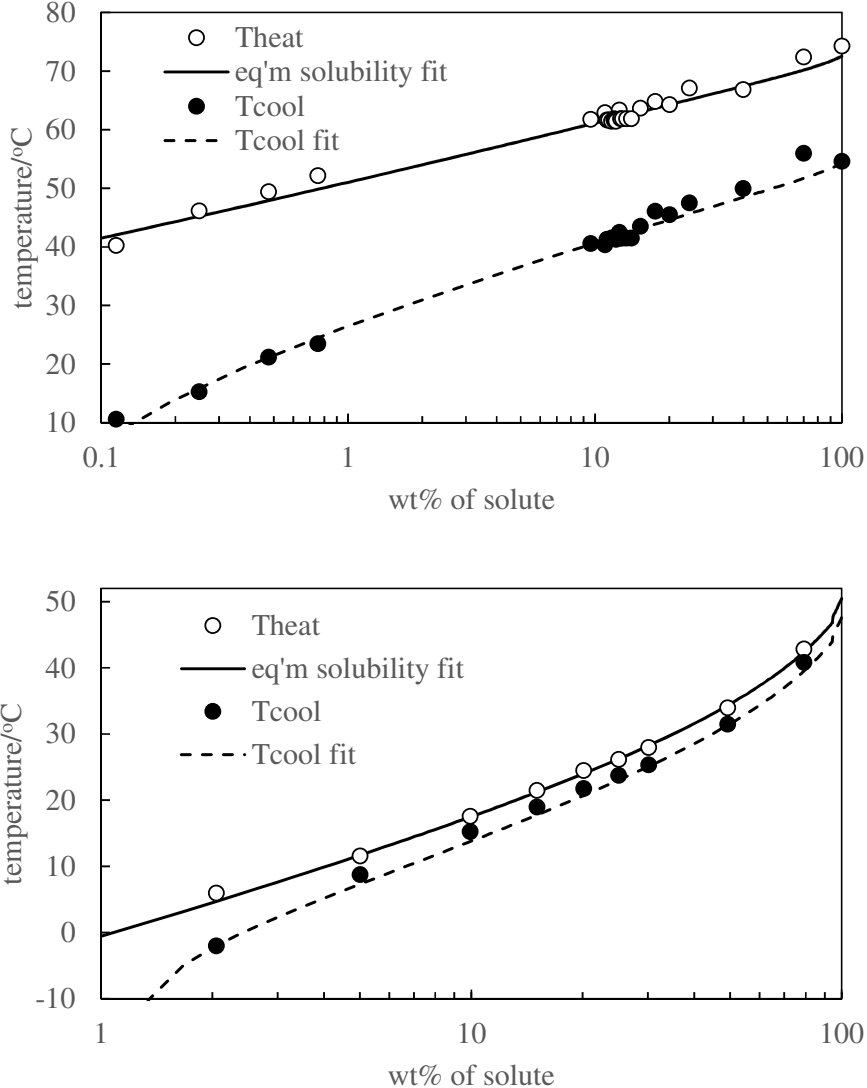


Figure 6. Pour point temperature versus solute concentration for SSS in CCC (upper plot, critical wt% = 12 wt%) and C24 in C7 (lower plot, critical wt% = 8.5 wt%).

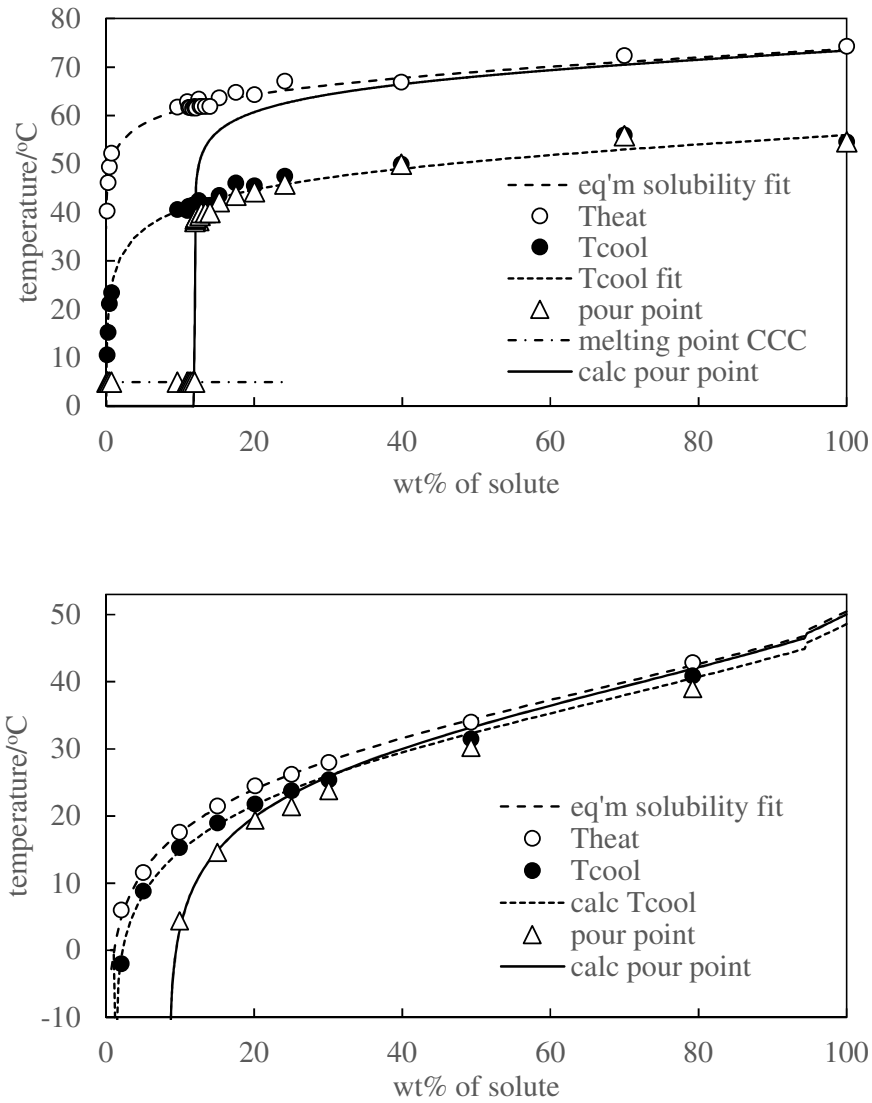
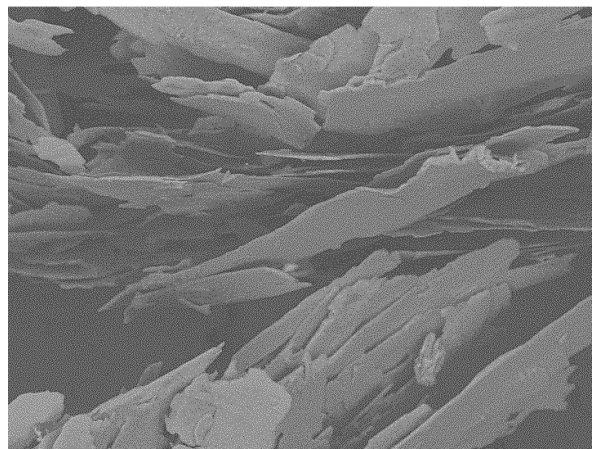
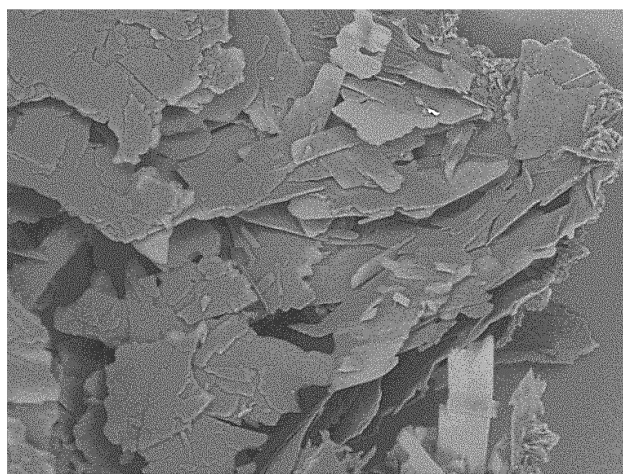


Figure 7. SEM images of extracted solute crystals.

- (i) C24 crystals extracted from a 20 wt% solution in heptane. Crystal extraction temperature = 20.0 °C, solubility boundary temperature = 24.5 °C and pour point temperature = 19.4 °C.

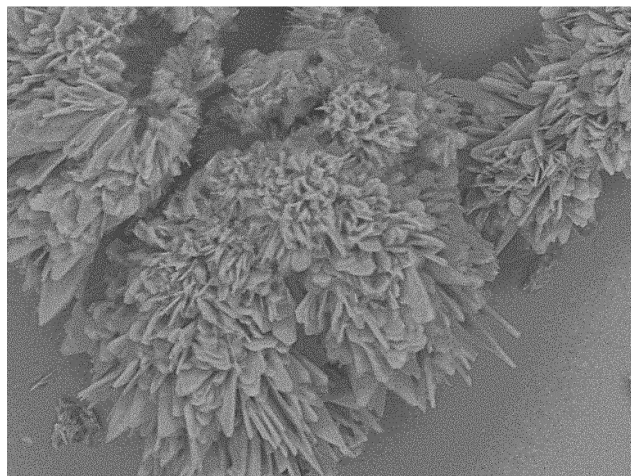


TM-1000_6371 2015/07/20 11:30 x600 100 um

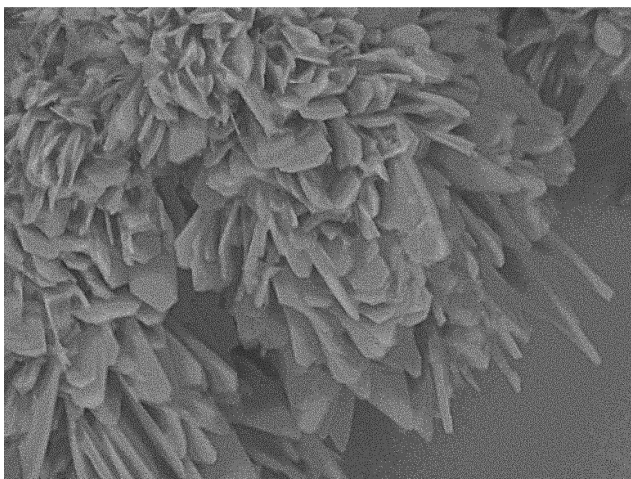


TM-1000_6369 2015/07/20 11:24 x400 200 um

- (ii) SSS crystals extracted from an 11 wt% solution in CCC. Crystal extraction temperature = 20.5 °C, solubility boundary temperature = 61.7 °C and pour point temperature = 5.0 °C.



TM-1000_6342 2015/07/17 13:19 x1.0k 100 um



TM-1000_6343 2015/07/17 13:22 x2.0k 30 um